Nanoscale

PAPER

View Article Online
View Journal | View Issue

Cite this: *Nanoscale*, 2022, **14**, 833

Tuning the local electronic structure of a single-site Ni catalyst by co-doping a 3D graphene framework with B/N atoms toward enhanced CO_2 electroreduction†

Tianyi Shao, ‡[a] Delong Duan,‡[a] Shengkun Liu,[a] Chao Gao, *[a] Hengxing Ji [a] and Yujie Xiong *[a,b]

Various single metal sites supported on N-doped carbon materials have been demonstrated to be effective catalysts for CO_2 electroreduction. However, it remains a challenging task to gain comprehensive understanding on how the local electronic structures of single metal catalytic sites are rationally tuned, which eventually holds the key to significantly enhance the electrocatalytic performance. Herein, we implement B–N bonds into an N-doped 3D graphene framework by B doping to further stabilize the supported catalytic Ni single-sites and simultaneously tune their local electronic structure. Moreover, electrochemical *in situ* Fourier-transform infrared spectroscopy reveals that the B–N bonds can further facilitate the production of pivotal *COOH intermediates in comparison with only N doping. As a result, the Ni single-site catalyst on the B, N co-doped 3D graphene framework achieves excellent catalytic performance with a CO faradaic efficiency (FE) of 98% and a turnover frequency (TOF) value of 20.1 s^{-1} at −0.8 V (*vs.* RHE), whereas the FE and TOF for the control sample without B doping are as low as 62% and 6.0 s^{-1}, respectively. This work highlights the superiority of modulating local electronic structures of single-site catalysts toward efficient electrocatalytic CO_2 reduction.

Received 5th October 2021,
Accepted 6th December 2021

DOI: 10.1039/d1nr06545a

rsc.li/nanoscale

Introduction

Great attention has been paid to carbon materials in the past few years due to their good stability and reactivity, especially in the field of supercapacitors[1,2] and H_2 evolution,[3] CO_2 reduction,[4,5] N_2 reduction,[6] O_2 reduction,[7–9] and O_2 evolution reactions.[10,11] Single-atom/site catalysts dispersed on carbon materials are able to realize the maximal atom utilization efficiency toward high catalytic performance. The common carbon-based single-atom/site catalysts for CO evolution through CO_2 electroreduction are porous carbon materials anchored with Fe, Co, and Ni single-atoms/sites. The general strategy for enhancing the catalytic performance is introducing N atoms to coordinate with catalytic metal sites in order to tune their local electronic structure inside the carbon skeleton.[12–14] In particular, implanting N atoms into the graphene skeleton results in the creation of more defects and the enrichment of more negative charges, thus regulating the electron density of catalytic metal sites.[15] Moreover, the strategy of integration with another metal atom has also been proven to tune the electronic structure of single-atom metal catalytic sites dispersed in the carbon network.[16,17] Although a few studies have shown that simultaneously doping two non-metallic elements in the carbon network could enable enhanced electrocatalytic performance, it still remains largely unexplored for tuning the CO_2 electroreduction reaction through co-doping two non-metallic heteroatoms in carbon-based single-atom/site catalysts.[18,19] To this end, we would like to explore the possibility of the strategy by incorporating another non-metallic heteroatom to tune the local electronic structure of single-atom metal catalytic sites in an N-doped carbon network toward enhanced catalytic performance in CO_2 electroreduction.

Given the low density, high aspect ratio, good conductivity, tunable channel structure, and abundant C/O functional groups as anchoring sites, 3D reduced graphene oxide (rGO) frameworks are theoretically regarded as the ideal support for various single-atom/site catalysts with a readily tunable coordi-

[a]*Hefei National Laboratory for Physical Sciences at the Microscale, School of Chemistry and Materials Science, University of Science and Technology of China, Hefei, Anhui 230026, China*
[b]*Institute of Energy, Hefei Comprehensive National Science Center, 350 Shushanhu Rd., Hefei, Anhui 230031, China. E-mail: yjxiong@ustc.edu.cn, gaoc@ustc.edu.cn*
†Electronic supplementary information (ESI) available: Supplementary experimental details, SEM images, HAADF-STEM images, XRD patterns, EXAFS data, XPS spectra and Auger electron spectra. See DOI: 10.1039/d1nr06545a
‡These authors contributed equally to this work.

nation environment toward various electrochemical reactions.[20,21] Herein, taking the single-site Ni catalyst supported on an N-doped 3D graphene framework as a model, we further incorporate B atoms into the catalyst system to tune the local electronic structure of single Ni catalytic sites in consideration of the distinct electronegativity between B and N.

In the traditional doping methods, single-atom/site catalysts supported on N-doped carbon networks are prepared by flowing ammonia gas, adding nitrogen-containing small organic molecules during the pyrolysis process, or directly pyrolyzing N-containing metal–organic frameworks.[22–24] Considering that the Ni single-site are anchored with the N atom, the doped B atom should be located nearby the N atom to form the B–N bond to precisely tune the local electronic structure of the single Ni catalytic sites. To this end, we utilize 1,4-benzenediboronic acid (BDBA) and *o*-phenylenediamine (*o*PD) as B and N sources to *in situ* grow polymer nanofibers along with the pore channel throughout the self-assembled three-dimensional (3D) graphene framework. In this way, the B–N bonds have been formed in advance and then the B and N can be doped simultaneously and adjacently in space during pyrolysis. The presence of B atoms not only facilitates the formation of Ni single-site catalysts, but also tunes their local electronic structure to promote the production of key *COOH intermediates in the CO_2 reduction reaction. Moreover, the long and continuous channel in the 3D graphene framework can promote the long-range diffusion and transport of CO_2 molecules. Consequently, as compared to the counterparts with only N doping, the single-site Ni catalyst supported on the B, N co-doped 3D graphene framework exhibits significantly enhanced catalytic performance in a wider applied voltage range.

Chao Gao

Chao Gao received his B.S. in chemistry in 2010 from Anhui Normal University, and his Ph.D. in inorganic chemistry in 2015 (with Professors Xingjiu Huang and Zhiyong Tang) from the University of Science and Technology of China (USTC). During his Ph.D. research, he had two years of training (2013–2015) with Professor Zhiyong Tang at the National Center for Nanoscience and Technology (NCNST). He is currently an Associate Professor in Professor Yujie Xiong's research team at the USTC. His current research interests are focused on the design and synthesis of photocatalysts, photoelectrodes and semi-artificial photosynthetic biohybrids for carbon dioxide reduction and methane conversion. He has published more than 40 scientific papers with over 4600 total citations (H-index 29). He was selected as a member of Youth Innovation Promotion Association CAS in 2021.

Experimental

Synthesis of the single-site Ni catalyst supported on a B, N co-doped 3D graphene framework

Graphene oxide (GO) was synthesized using the modified Hummers' method. The self-assembled 3D graphene framework loaded with the B, N-containing polymer and Ni sites was prepared by a facile hydrothermal method. First, 0.3 mL of 10 mM $Ni(NO_3)_2{\cdot}6H_2O$ and 25 μL of 30% H_2O_2 were added into 10 mL of 0.3 wt% GO solution under general sonication for 30 min. Then the solution was immediately transferred to an ultrasonic cell disruption system for another vigorous 45 min sonication (solution A). Second, the two small organic molecules of *o*PD and BDBA with various ratios were fully dissolved in 20 mL of mixed solvent containing 15 mL of ethanol and 5 mL of H_2O (solution B). The two solutions A and B obtained above were mixed together and heated at 180 °C for 12 h by a hydrothermal method. After slowly cooling down to room temperature, the obtained self-assembled 3D graphene framework with a cylinder shape was put into a vacuum oven to remove most of the ethanol, followed by freezing dry with liquid nitrogen to achieve complete dryness. The single-site Ni catalysts supported on the B, N co-doped 3D graphene framework with different B/N ratios were finally obtained *via* pyrolyzing at 820 °C (heating rate: 5 °C min^{-1}) under a flowing Ar atmosphere for 3 h in a tube furnace. The obtained single-site Ni catalysts supported on the B, N co-doped 3D graphene framework with different B/N ratios (BDBA/*o*PD, 0/0.6, 0.1/0.5, 0.2/0.4, 0.3/0.3, 0.4/0.2, and 0.6/0, mmol $mmol^{-1}$) were denoted as Ni–N_6, Ni–B_1N_5, Ni–B_2N_4, Ni–B_3N_3, Ni–B_4N_2, and Ni–B_6, respectively.

X-ray absorption fine structure (XAFS) characterization

Ni K-edge XAFS characterization was performed at the beamline 1 W2B of Beijing Synchrotron Radiation Facility (BSRF), China. The acquired K-edge extended XAFS (EXAFS) data were treated through the Demeter package, and the processed curve was compared with standard samples of Ni foil, NiO, and nickel(II) phthalocyanine. Ni K-edge X-ray absorption near-edge structure (XANES) simulations based on the self-consistent multiple-scattering theory were performed using FEFF 8.2 code. The N and B K-edge XAFS characterization was performed at the MCD Endstation of the BL12B-a Soft X-Ray beamline at the National Synchrotron Radiation Laboratory (NSRL) in Hefei, China.

Evaluation of the catalytic performance for CO_2 electroreduction

Electrochemical measurements, including CO_2 electroreduction and linear sweep voltammetry (LSV), were carried out on an electrochemical station (CHI660D) with a conventional H-type electrochemical cell, in which the cathode and anode

in the CO_2-saturated 0.5 M $KHCO_3$ electrolyte (pH = 7.2) were separated by a Nafion117 membrane. The three-electrode system consisted of a platinum plate as the counter electrode, an Ag/AgCl (saturated KCl) as the reference electrode, and carbon paper as the working electrode. In a typical preparation for the working electrode, 5 mg of the sample and 50 μL of Nafion solution (5 wt%) were uniformly dispersed in 1 mL of water–ethanol solution with the volume ratio of 1 : 3 by sonication. The catalyst ink was dropped onto the two sides of a carbon paper electrode with a catalyst loading of 0.5 mg cm^{-2}. The working electrode was dried in a vacuum oven overnight. All potentials in this study were measured against the Ag/AgCl reference electrode and converted to the RHE reference scale using E (*vs.* RHE) = E (*vs.* Ag/AgCl) + 0.1989 V + 0.059 × pH. The amounts of CO and H_2 were measured using a gas chromatograph (GC, 7890A, Ar carrier, Agilent). H_2 was detected with a thermal conductivity detector (TCD), and CO was detected with a flame ionization detector (FID).

Electrochemical *in situ* Fourier-transform infrared (FTIR) spectroscopy

Electrochemical *in situ* FTIR spectra were recorded with a Fourier transform spectrometer (Bruker VERTEX 70v/s) equipped with a KBr beam splitter and various detectors connected with an infrared microscope (Bruker Hyperion 2000, ×50 objective) at the Infrared Spectroscopy and Microspectroscopy Endstation (BL01B) in the National Synchrotron Radiation Laboratory (NSRL) in Hefei, China. The catalysts were uniformly covered on the glassy carbon electrode equipped in the *in situ* electrochemical cell, which was filled with CO_2-saturated 0.5 M $KHCO_3$ solution. The window of the *in situ* electrochemical cell was covered by a CaF_2 plate. Note: Ensure that the electrolyte existing between the CaF_2 plate and glassy carbon electrode is a very thin layer since the infrared signals are easily disturbed by water. The *in situ* electrochemical cell was connected to an electrochemical station during the process of the electrocatalytic CO_2 reduction. The spectrum of the sample before applying with voltage was deducted as the background signal, and the time-dependent measurements were performed under a fixed potential.

Results and discussion

To prepare the model catalyst, a one-step hydrothermal process is primarily developed to obtain the 3D self-assembled rGO framework with the B, N-containing polymer, showing the shape of a cylinder (Fig. S1†). Generally speaking, the N-containing monomer *o*PD tends to dehydrogenize and self-polymerize to form long and wide nanofibers (Fig. 1a and S2†).[25] After integrating the *o*PD with B-containing BDBA, the unidirectional chain growth is suppressed while the dendronized copolymerization is facilitated (Fig. S3†), producing shorter and more slender nanobelts (Fig. 1e and S4†). Such a morphological change suggests the successful introduction of B–N bonds into the polymer by the copolymerization of *o*PD and BDBA precursors. In contrast, the single BDBA as the reactant monomer produces the sheet-shape polymer embedded into the 3D graphene network (Fig. S5†).[26] The obtained cylinder graphene is further treated under oriented freeze drying from bottom to top so that the tiny ice nucleus would grow along the longitudinal direction through the internal mesopores to form parallel ice columns. Then the crisscrossing and interlaced channels with long-range alignment are created across the whole graphene framework. Finally, the single-site Ni catalysts supported on the B, N co-doped 3D graphene framework are obtained by pyrolyzing the cylinder graphene at 820 °C under a flowing Ar atmosphere for 3 hours to firmly anchor the atomically dispersed Ni sites by the surrounding doped N and B heteroatoms. As shown in Fig. 1b, 1f, and S6† the interlaced channels are kept for the graphene framework after pyrolysis, which would facilitate the diffusion and transport of CO_2 molecules. The Brunauer–Emmett–Teller (BET) surface area is obtained by analysis of N_2 absorption-desorption isotherms (Fig. S7†). Compared to the sample with only N doping (Ni–N_6), the BET surface area of the sample with the B, N co-doped graphene framework (Ni–B_2N_4) is significantly reduced (322.6 m^2 g^{-1} *vs.* 87.4 m^2 g^{-1}), most likely as the interspaces of the graphene framework are partially filled with the carbonized fiber fragments. In addition, transmission electron microscopy (TEM) images (Fig. 1c and g) further show that the graphene maintains a sheet-like structure with crimps and wrinkles after pyrolysis, and no Ni-derived clusters or particles are observed on the nanosheets. To resolve information at an atomic scale, aberration-corrected high-angle annular dark-field scanning TEM (HAADF-STEM) is further used to characterize the dispersion of the Ni sites. For the sample with only N doping (Ni–N_6), it clearly exhibits the primary existence of single Ni atoms but simultaneously the presence of a few Ni nanoparticles as highlighted by the yellow circles (Fig. 1d and S8†). In contrast, for the sample with B, N co-doped graphene nanosheets (Ni–B_2N_4), it demonstrates the uniform distribution of isolated Ni atoms without the presence of Ni nanoclusters or nanoparticles (Fig. 1h and S9†), inferring that the introduction of B can effectively avoid metal agglomeration. The loading amounts of Ni sites are quantified by inductively coupled plasma-atomic emission spectroscopy (ICP-AES), showing that the doped graphene framework samples have similar Ni contents of about 0.5% (Table S1†). To further confirm whether the metal nanoparticles are embedded within the graphene framework during the hydrothermal and pyrolysis process, X-ray diffraction (XRD) is performed and no characteristic peak assigned to Ni nanoparticles (PDF 04-0850) is observed in the obtained XRD patterns (Fig. S10†). The three peaks in the ranges of 20–30°, 40–45°, and 53–58° are related to the (111), (100), and (222) planes of graphene (PDF# 75-2078), respectively. The elemental energy-dispersive X-ray spectroscopy (EDS) mapping analysis illustrates the homogeneous dispersion of B, C, N, O, and Ni elements (Fig. 1i), further confirming that B and N have been uniformly doped into the graphene skeleton. The practical B/N ratios and their doping percentages in the samples are analyzed by X-ray photoelectron

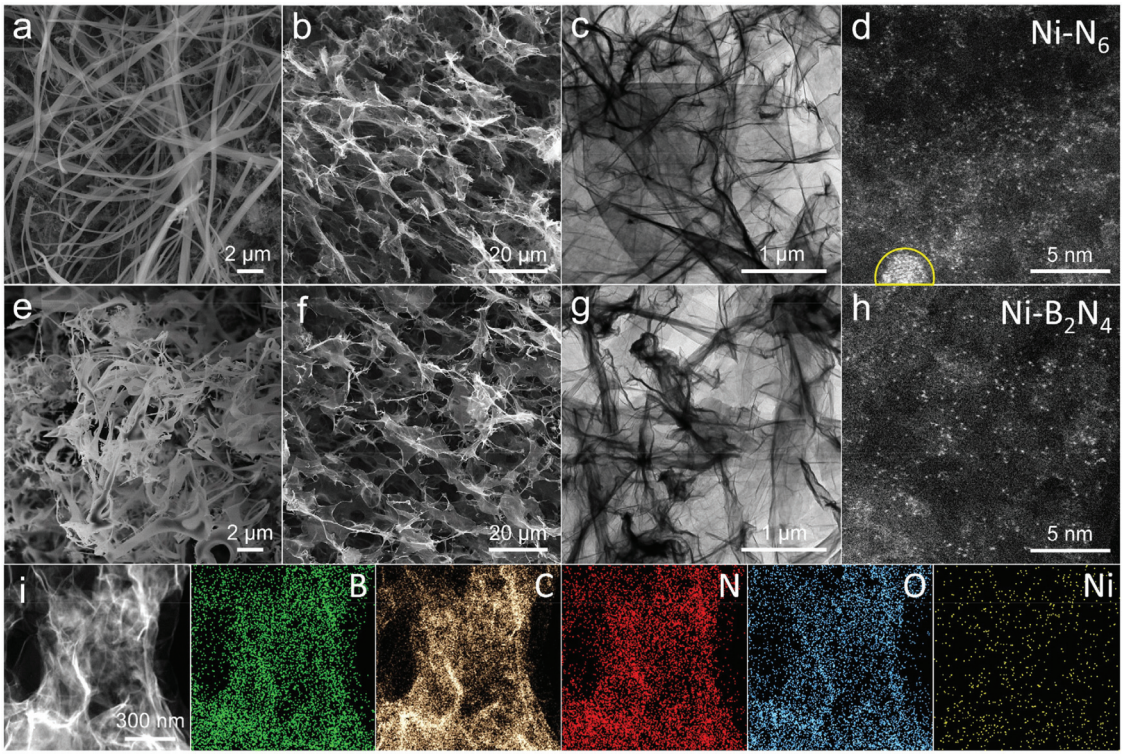

Fig. 1 (a) Scanning electron microscopy (SEM) images of the 3D graphene framework loaded with the N-containing polymer and Ni sites. SEM images (b), TEM images (c), and aberration-corrected HAADF-STEM images (d) of the Ni–N_6 sample. (e) SEM images of the 3D graphene framework loaded with the B, N-containing polymer and Ni sites. SEM images (f), TEM images (g), and aberration-corrected HAADF-STEM images (h) of the Ni–B_2N_4 sample. (i) The EDS mapping of B, C, N, O, and Ni in the Ni–B_2N_4 sample.

spectroscopy (XPS) characterization, revealing that the practical B/N ratios indeed are promoted by increasing BDBA/*o*PD ratios (Table S2†). In particular, the Ni–B_2N_4 sample has a doping percentage of 1.73% and 5.09% in weight for B and N, respectively.

Upon directly observing the existence of the single Ni atom from the HAADF images above, X-ray absorption spectroscopy (XAS) is implemented to understand the valence states and refined coordination environments. In the XANES spectra (Fig. 2a), the Ni absorption edge of single-site Ni catalysts supported on the B, N co-doped 3D graphene framework with different B/N ratios is located in the range of Ni foil (0) and NiO (+2), indicating that the single Ni site possesses a $+\delta$ ($0 < \delta < 2$) valence state in their structural units.[27] In the Fourier transform EXAFS (FT-EXAFS) spectra (Fig. 2b), the manifested dominant peaks at about 1.4 Å are assigned to the direct coordination of single Ni sites with N/O/C atoms in the nearest coordination position, while the peaks at about 2.0 Å are assigned to the chemical interactions for single Ni sites with B/C atoms in a bit further distance. The intensity of the peak at about 1.4 Å has a positive correlation with the coordination numbers of Ni sites. Compared with the sample with only N doping (Ni–N_6), the introduction of B atoms into the graphene network enhances the peak intensity at about 1.4 Å, indicating the increased coordination numbers of Ni sites that could contribute to stabilizing the single sites. Moreover, the peak at 2.2 Å, attributed to the Ni–Ni bond in Ni foil, is not obviously observed in the profiles of all the samples, which further corroborates the atomic dispersion of Ni sites.

To acquire the precise coordination structures, the EXAFS fitting and optimized configuration (Fig. S11 and Table S3†) are simulated by referring to the fixed standard samples of Ni foil, NiO, and nickel phthalocyanine (NiPc). The fitting results indicate that the Ni sites in the N doped or B, N co-doped samples are coordinated with nearly three neighbouring N/O/C atoms (note that the C/N/O light elements could not be distinguished clearly by EXAFS spectra). Notably, the lowest coordination number of Ni sites for the sample with only B doping (Ni–B_6) suggests that the B atoms are not ideal anchoring sites for single Ni sites. Thus the Ni–N/O/C coordination numbers first increase and then decrease with the increasing content of the B precursor, as the introduced B could regulate the local electronic structure to more firmly coordinate with Ni sites while the increased B/N ratio would reduce the number of N anchoring sites to coordinate with Ni sites. In particular, the Ni–B_2N_4 sample possesses the maximal coordination number, which is in accordance with the peak intensity in EXFAS spectra (Fig. 2b).

The above results demonstrate that the incorporation of the B atom is vital for regulating the coordination numbers and thus the local electronic structure of the single Ni catalytic sites, which may significantly influence the electrocatalytic

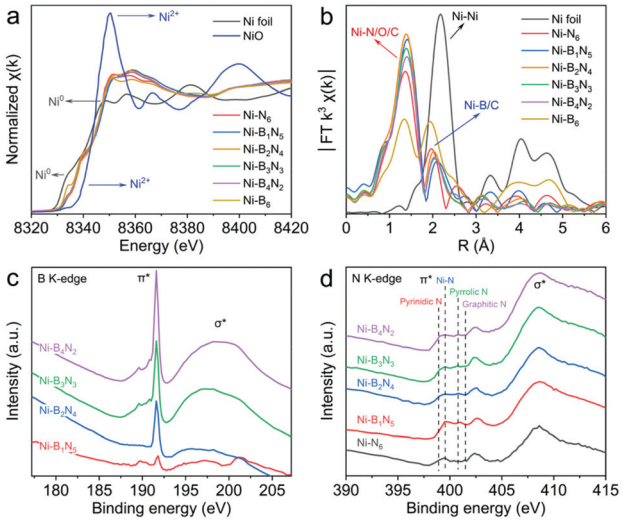

Fig. 2 XAS spectra for the Ni–B_xN_{6-x} (x = 0–6) samples. (a) Normalized Ni K-edge XANES spectra. (b) k^3-Weighted Ni K-edge FT-EXAFS spectra. (c) B K-edge XANES spectra. (d) N K-edge XANES spectra.

performance for CO_2 reduction. To precisely account for the electronic structure, XANES spectra for B and N are taken into consideration to analyze the doping features in the graphene framework. The B K-edge spectra exhibit sharp peaks at 191.7 eV (1s → π*) and broad bands between 196.7 and 201.3 eV (1s → σ*), which are attributable to the typical resonances of sp^2-hybridized B–N bonds (Fig. 2c).[28,29] These characteristic signals undoubtedly affirm the formation of B–N moieties inside the graphene network. In addition, the corresponding information of N with π* and σ* features is evaluated by N K-edge spectra (Fig. 2d).[29] The results suggest that there are multiple types of N species, including pyridinic N, Ni–N, pyrrolic N, graphitic N, and oxidized N. In particular, the observed peak assigned to the Ni–N bond at about 399.5 eV suggests that the single Ni sites are directly coordinated with N atoms.

To further elucidate the variation of the local coordination environment and electronic structure by B doping, the XPS characterization is analyzed to investigate the various N and B species in the samples (Fig. 3). For N 1s XPS spectra (Fig. 3a–e), the N 1s peak can be fitted to six characteristic peaks, including N–B (397.8 eV), pyridinic N (398.5 eV), Ni–N (399.4 eV), pyrrolic N (400.6 eV), graphitic N (401.3 eV), and oxidized N (402.8 eV).[29,30] Remarkably, with the addition of the B precursor (BDBA), the proportions of pyrrolic N and Ni–N increase, while the proportions of pyridinic N and graphitic N decrease. The increased percentage of pyrrolic N originates from the incorporation of B into the graphene lattice network by taking full advantage of the chemical interaction between $-NH_2$ and $-B-(OH)_2$ functional group to form a five-membered ring. Among all the samples, the Ni–B_2N_4 has the highest ratio of pyrrolic N. For the B 1s XPS spectra (Fig. 3f), the intensities of the peak for B–N (191.6 eV) increase with increasing B/N ratios, further confirming the formation of B–N bonds in the graphene framework.[29,31–33] The peak of the B–O bond (193.0 eV) for the Ni–B_6 sample is derived from the $-B(OH)_2$ group in BDBA. For the Ni XPS signal of the samples (Fig. S12a†), the binding energy of the Ni $2p_{3/2}$ is situated higher than that of Ni^0 (582.6 eV) and lower than that of Ni^{2+} (855.6 eV),[27] suggesting that the valence state of Ni sites is between Ni^0 and Ni^{2+}. This result is in agreement with the conclusion from the XANES characterization. In addition, the binding energy of the Ni $2p_{3/2}$ slightly shifts to a higher binding energy, indicating

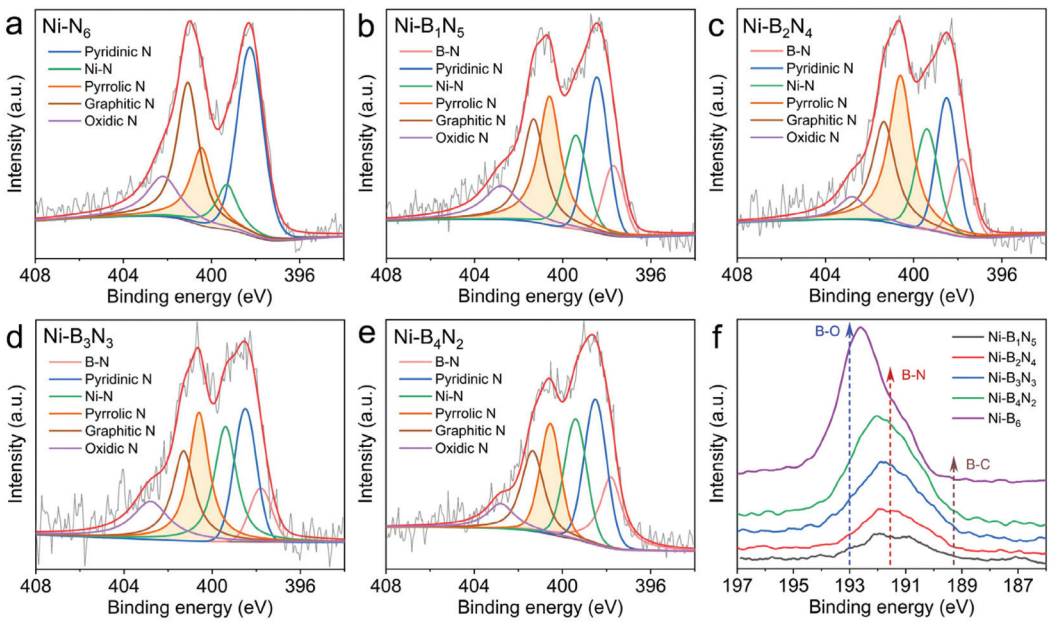

Fig. 3 High-resolution N 1s (a–e) and B 1s (f) XPS spectra of the Ni–B_xN_{6-x} (x = 0–6) samples.

that the valence state of Ni sites increases with increasing B/N ratios. This result is also confirmed by the Ni Auger electron spectra (Fig. S12b†). The main peak of Ni–B_2N_4 shifts to a higher binding energy in comparison with Ni–N_6, confirming that the valence state of Ni sites increases after B doping. From the above information, the addition of B leads to the formation of B–N bonds that induces the redistribution of charges on Ni sites, thus regulating the local electronic structure of single Ni sites.

Upon acquiring the key information of single-site Ni catalysts supported on the B, N co-doped 3D graphene framework, we are now in a position to evaluate their performance as electrocatalysts for CO_2 reduction as well as validate the role of the B-tuned local electronic structure in CO_2 electroreduction. As revealed by linear sweep voltammetry (LSV) curves in Fig. 4a, the current densities of Ni–B_xN_{6-x} (x = 1–5) are apparently higher than those of the Ni–N_6 and Ni–B_6 samples and the Ni–B_2N_4 exhibits the highest current density, demonstrating that the addition of B could significantly enhance the catalytic performance for CO_2 electroreduction. The products are CO and H_2, without other detectable carbonaceous products in the CO_2-saturated 0.5 M $KHCO_3$ electrolyte. Moreover, the faradaic efficiencies (FEs) for CO evolution (Fig. 4b) are recorded at different applied potentials from −0.5 to −1.1 V (*vs.* RHE). The Ni–B_2N_4 sample exhibits the optimal CO FE of 98% at −0.8 V with a remarkable CO selectivity over 90%, as well as the widest range of working potentials. In sharp contrast, the Ni–N_6 sample demonstrates poor activity toward CO generation. To directly compare the catalytic performance, the turnover frequency (TOF), referring to the number of produced CO per Ni single-site in unit time, is calculated on the basis of total Ni mass loaded on carbon fiber paper (Fig. 4c). The Ni–B_2N_4 reaches the highest TOF value of 20.1 s^{-1} at −0.8 V, while the TOF value for Ni–N_6 is as low as 6.0 s^{-1}.[14,16] Meanwhile, the other counterpart samples with various B contents also manifest significantly higher catalytic performance in comparison with Ni–N_6, confirming the tuned local electronic structure by B doping plays a vital role in improving the catalytic performance for CO_2 electroreduction. Accordingly, the long-term stability for 20 h continuous measurement confirms that Ni–B_2N_4 possesses obviously higher steady current density and selectivity toward CO generation (Fig. 4d). The Ni sites coordinated with pyrrolic N have been proven to be closely correlated with the catalytic performance for CO_2 electroreduction to CO.[34] Considering that Ni–B_2N_4 has the highest ratio of pyrrolic N and the highest catalytic performance toward CO_2 electroreduction, it is supposed that the Ni single-site coordinated with pyrrolic N contributes to the high catalytic performance in CO_2 electroreduction. Overall, doping B into the single-site Ni catalyst supported on the N-doped 3D graphene framework enables to modulate the local coordination environment and electronic structure of the Ni catalytic sites, which plays an important role in endowing the remarkable improvement of catalytic performance for CO_2 electroreduction.

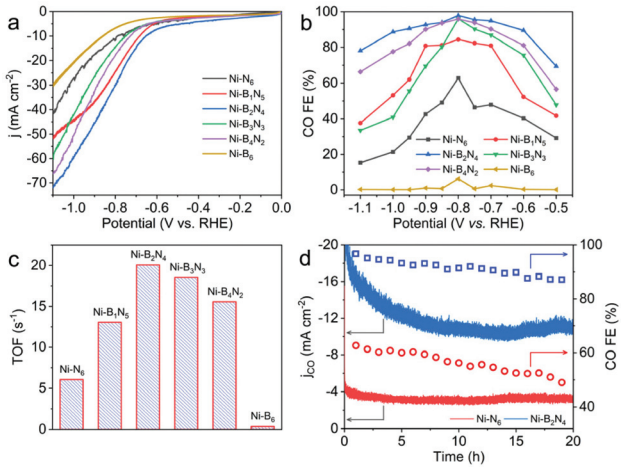

Fig. 4 (a) LSV curves for the Ni–B_xN_{6-x} (x = 0–6) samples in the 0.5 M CO_2-saturated $KHCO_3$ electrolyte. (b) FEs of CO at different applied potentials for the Ni–B_xN_{6-x} (x = 0–6) samples. (c) The corresponding TOFs of CO production at −0.8 V for the Ni–B_xN_{6-x} (x = 0–6) samples. (d) Long-term stability measurement of Ni–N_6 and Ni–B_2N_4 at −0.8 V for 20 h.

The overall electrochemical reaction for the reduction of CO_2 to CO can be described as the following three elementary steps:[35]

$$CO_2(g) + H^+ + * + e^- \rightarrow *COOH \quad (1)$$

$$*COOH + H^+ + e^- \rightarrow *CO + H_2O(l) \quad (2)$$

$$*CO \rightarrow CO(g) + * \quad (3)$$

where * denotes an adsorption site. To further understand the role of B doping on the reaction pathway, synchrotron radiation-based electrochemical *in situ* Fourier transform infrared (FTIR) spectroscopy is employed to examine the intermediates during the CO_2 electroreduction reaction. Prior to the *operando* measurements, FTIR spectra of all the samples after pyrolysis are shown in Fig. 5a, which show three typical peaks of the rGO nanosheet, including the peaks at 3439 cm^{-1} assigned to the O–H stretching vibration, 1562 cm^{-1} attributed to the C=C stretching vibration, and 1166 cm^{-1} ascribed to the C–O stretching vibration.[31,32] For the *in situ* CO_2 electroreduction on various samples (Fig. 5b–h), there is no observable signal at the beginning of the CO_2 electroreduction reactions, and all the peaks related to the intermediate in the spectral data are gradually enhanced with increasing electrolysis time. As the key intermediate in CO_2 electroreduction to CO, the *COOH has four characteristic peaks referring to 3550 cm^{-1} (O–H symmetric stretching), 1680 cm^{-1} (C=O symmetric stretching), 1360 cm^{-1} (O–H in-plane bending), and 1160 cm^{-1} (C–O symmetric stretching). The sample of rGO (Fig. 5b) with no capability of CO_2 electroreduction barely shows any signal of the stretching vibration of O–H and C=O. In stark contrast, these two prominent peaks for the Ni–B_xN_{6-x} (x = 1–5) samples (Fig. 5d–g) are substantially sharper than the Ni–N_6 (Fig. 5c) and Ni–B_6 (Fig. 5h) counterpart, which is in good accordance with the catalytic performance shown in Fig. 4. The enhanced

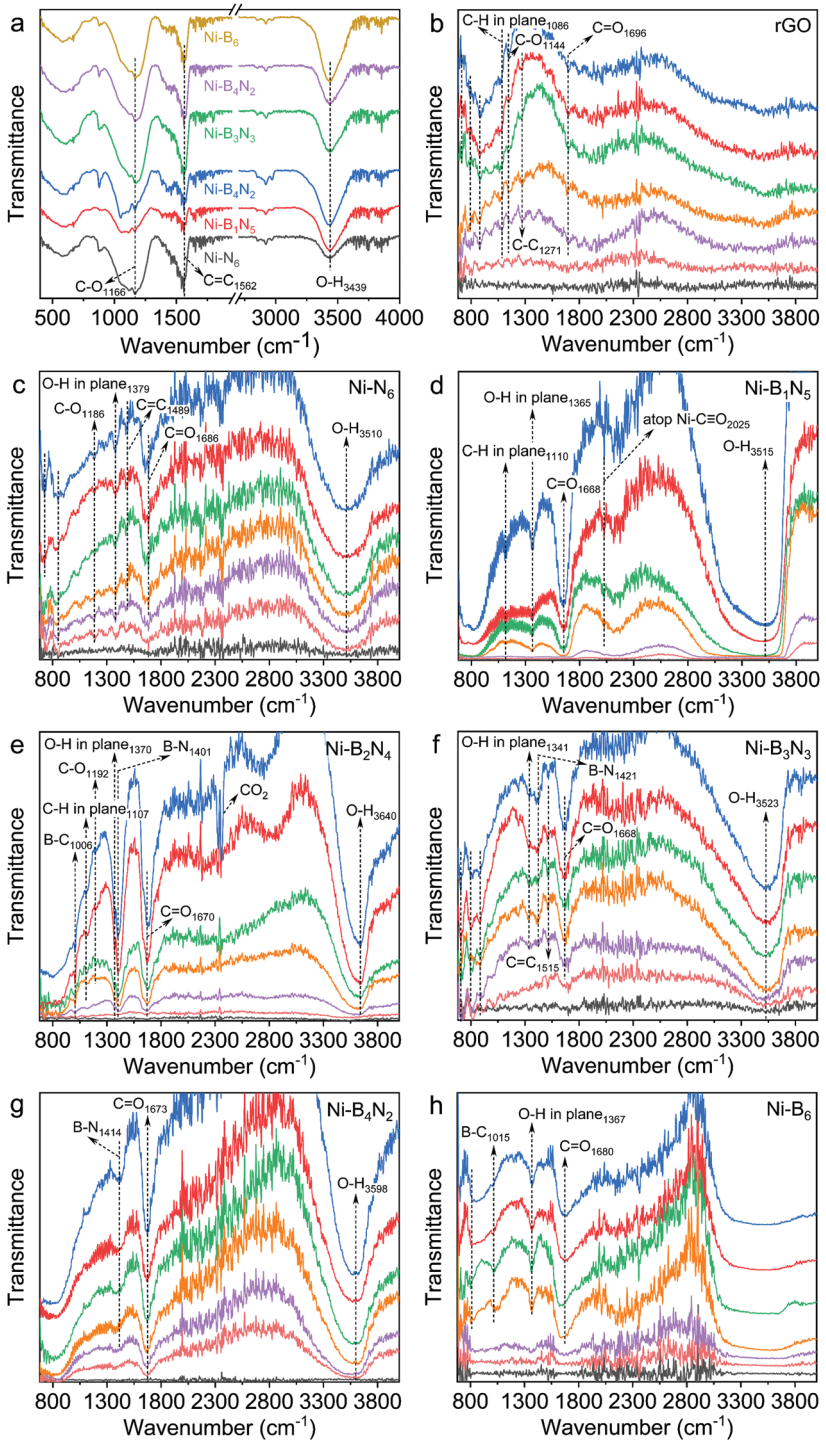

Fig. 5 (a) FTIR spectra of the Ni–B_xN_{6-x} (x = 0–6) samples. (b–h) Electrochemical *in situ* FTIR spectra of the Ni–B_xN_{6-x} (x = 0–6) samples at the same potential (−0.8 V *vs.* RHE). The curves from bottom to top in each panel refer to the different reaction time of 0, 1, 2, 3, 5, 7, and 10 min, respectively.

signal suggests that the production of the *COOH intermediate, the rate-determining step in CO_2 electroreduction to CO, is remarkably promoted to give a higher content. In addition, especially for the Ni–B_2N_4 sample, a strong stretching peak ascribed to the B–N bond is clearly observed at 1410 cm^{-1} and changes significantly over time, suggesting that the formed B–N bonds after B doping modulate the local electronic structure of Ni active sites and are involved in the CO_2 reduction reaction dynamically. To sum up, the coordination environment, or exactly the local electronic structure of Ni sites could alter

the adsorption free energy of the intermediates to facilitate the CO_2 reduction.[36] In our work, the introduction of B modulates the local electronic structure of Ni catalytic sites to facilitate the production of key *COOH intermediates and consequently lowers the energy barrier in the CO_2 reduction reaction, thereby boosting the catalytic performance for CO_2 electroreduction.

Conclusions

In summary, a synthetic strategy for *in situ* growing polymer nanofibers along the internal channel of a self-assembled 3D graphene framework has been developed for constructing a B, N co-doped 3D graphene framework coupled with a single-site Ni catalyst. Through the technique of directional freeze drying, the graphene framework treated by pyrolysis possesses continuous channels to favor the diffusion of CO_2 to catalytic sites, as well as the release of produced CO molecules. The incorporated B atoms play a crucial role in promoting the atomization of Ni single-sites and significantly impact their electronic structure by modifying the local coordination environment. As a result, the doped B atoms markedly enhance the quantity of Ni single-sites that are coordinated with adjacent pyrrolic N, which are supposed to be responsible for the improved catalytic performance in CO_2 electroreduction. Additionally, the formation of B–N bonds detected by *in situ* FTIR may contribute to facilitate the production of key *COOH intermediates. The appropriate ratio of B and N is also proven to be essential for outstanding catalytic performance. This work not only demonstrates a strategy for tuning the local electronic structure of single metal catalytic sites on 3D graphene frameworks, but also highlights the importance of modulating the local electronic structure of single-site catalysts toward enhanced performance.

Author contributions

T. S. designed and performed the experiments, analyzed and discussed the experimental results, and drafted the manuscript. D. D. performed the XAFS characterization and analyzed the results. S. L. joined the discussion of experiments and data. C. G. and Y. X. proposed the research direction, supervised the project, analyzed and discussed the experimental results, and revised the manuscript.

Conflicts of interest

There are no conflicts to declare.

Acknowledgements

This work was supported by the National Key R&D Program of China (2020YFA0406103), NSFC (21725102, 91961106, and 91963108), DNL Cooperation Fund, CAS (DNL201922), and Youth Innovation Promotion Association CAS. Ni K-edge XAFS characterization was performed at the beamline 1W2B of Beijing Synchrotron Radiation Facility (BSRF), China. N and B K-edge XAFS characterization was performed at the MCD Endstation (BL12B) in the National Synchrotron Radiation Laboratory (NSRL) in Hefei, China. Electrochemical *in situ* FTIR data were obtained at the Infrared Spectroscopy and Microspectroscopy Endstation (BL01B) in the National Synchrotron Radiation Laboratory (NSRL) in Hefei, China. We thank the support from USTC Center for Micro- and Nanoscale Research and Fabrication.

Notes and references

1 S.-C. Li, B.-C. Hu, Y.-W. Ding, H.-W. Liang, C. Li, Z.-Y. Yu, Z.-Y. Wu, W.-S. Chen and S.-H. Yu, *Angew. Chem., Int. Ed.*, 2018, **57**, 7085–7090.
2 Y. Zhao, C. Hu, Y. Hu, H. Cheng, G. Shi and L. Qu, *Angew. Chem., Int. Ed.*, 2012, **51**, 11371–11375.
3 L. Cao, Q. Luo, W. Liu, Y. Lin, X. Liu, Y. Cao, W. Zhang, Y. Wu, J. Yang, T. Yao and S. Wei, *Nat. Catal.*, 2019, **2**, 134–141.
4 L. Ye, Y. Ying, D. Sun, Z. Zhang, L. Fei, Z. Wen, J. Qiao and H. Huang, *Angew. Chem., Int. Ed.*, 2020, **59**, 3244–3251.
5 D. Hursan, A. A. Samu, L. Janovak, K. Artyushkova, T. Asset, P. Atanassov and C. Janaky, *Joule*, 2019, **3**, 1719–1733.
6 Y. Liu, Q. Li, X. Guo, X. Kong, J. Ke, M. Chi, Q. Li, Z. Geng and J. Zeng, *Adv. Mater.*, 2020, **32**, 1907690.
7 X. Xie, C. He, B. Li, Y. He, D. A. Cullen, E. C. Wegener, A. J. Kropf, U. Martinez, Y. Cheng, M. H. Engelhard, M. E. Bowden, M. Song, T. Lemmon, X. S. Li, Z. Nie, J. Liu, D. J. Myers, P. Zelenay, G. Wang, G. Wu, V. Ramani and Y. Shao, *Nat. Catal.*, 2020, **3**, 1044–1054.
8 L. Jiao, J. Li, L. L. Richard, Q. Sun, T. Stracensky, E. Liu, M. T. Sougrati, Z. Zhao, F. Yang, S. Zhong, H. Xu, S. Mukerjee, Y. Huang, D. A. Cullen, J. H. Park, M. Ferrandon, D. J. Myers, F. Jaouen and Q. Jia, *Nat. Mater.*, 2021, **20**, 1385–1391.
9 Y. Qu, Z. Li, W. Chen, Y. Lin, T. Yuan, Z. Yang, C. Zhao, J. Wang, C. Zhao, X. Wang, F. Zhou, Z. Zhuang, Y. Wu and Y. Li, *Nat. Catal.*, 2018, **1**, 781–786.
10 H. Fei, J. Dong, Y. Feng, C. S. Allen, C. Wan, B. Volosskiy, M. Li, Z. Zhao, Y. Wang, H. Sun, P. An, W. Chen, Z. Guo, C. Lee, D. Chen, I. Shakir, M. Liu, T. Hu, Y. Li, A. I. Kirkland, X. Duan and Y. Huang, *Nat. Catal.*, 2018, **1**, 63–72.
11 J. Wang, S.-J. Kim, J. Liu, Y. Gao, S. Choi, J. Han, H. Shin, S. Jo, J. Kim, F. Ciucci, H. Kim, Q. Li, W. Yang, X. Long, S. Yang, S.-P. Cho, K. H. Chae, M. G. Kim, H. Kim and J. Lim, *Nat. Catal.*, 2021, **4**, 212–222.
12 X. Wang, Z. Chen, X. Zhao, T. Yao, W. Chen, R. You, C. Zhao, G. Wu, J. Wang, W. Huang, J. Yang, X. Hong, S. Wei, Y. Wu and Y. Li, *Angew. Chem., Int. Ed.*, 2018, **57**, 1944–1948.

13 J. Gu, C.-S. Hsu, L. Bai, H. Chen and X. Hu, *Science*, 2019, **364**, 1091–1094.
14 T. Zheng, K. Jiang, N. Ta, Y. Hu, J. Zeng, J. Liu and H. Wang, *Joule*, 2019, **3**, 265–278.
15 W. Ni, Z. Liu, Y. Zhang, C. Ma, H. Deng, S. Zhang and S. Wang, *Adv. Mater.*, 2021, **33**, 2003238.
16 Y.-N. Gong, L. Jiao, Y. Qian, C.-Y. Pan, L. Zheng, X. Cai, B. Liu, S.-H. Yu and H.-L. Jiang, *Angew. Chem., Int. Ed.*, 2020, **59**, 2705–2709.
17 J. Pei, T. Wang, R. Sui, X. Zhang, D. Zhou, F. Qin, X. Zhao, Q. Liu, W. Yan, J. Dong, L. Zheng, A. Li, J. Mao, W. Zhu, W. Chen and Z. Zhuang, *Energy Environ. Sci.*, 2021, **14**, 3019–3028.
18 S. Wang, L. Zhang, Z. Xia, A. Roy, D. W. Chang, J.-B. Baek and L. Dai, *Angew. Chem., Int. Ed.*, 2012, **51**, 4209–4212.
19 J. Zhang, L. Qu, G. Shi, J. Liu, J. Chen and L. Dai, *Angew. Chem., Int. Ed.*, 2016, **55**, 2230–2234.
20 H. Sun, Z. Xu and C. Gao, *Adv. Mater.*, 2013, **25**, 2554–2560.
21 K. Pang, X. Song, Z. xu, X. Liu, Y. Liu, L. Zhong, Y. Peng, J. Wang, J. Zhou, F. Meng, W. Jian and C. Gao, *Sci. Adv.*, 2020, **6**, eabd4045.
22 X. Zu, X. Li, W. Liu, Y. Sun, J. Xu, T. Yao, W. Yan, S. Gao, C. Wang, S. Wei and Y. Xie, *Adv. Mater.*, 2019, **31**, 1808135.
23 J. Yang, Z. Qiu, C. Zhao, W. Wei, W. Chen, Z. Li, Y. Qu, J. Dong, J. Luo, Z. Li and Y. Wu, *Angew. Chem., Int. Ed.*, 2018, **57**, 14095–14100.
24 Y. Zhao, H. Zhou, X. Zhu, Y. Qu, C. Xiong, Z. Xue, Q. Zhang, X. Liu, F. Zhou, X. Mou, W. Wang, M. Chen, Y. Xiong, X. Lin, Y. Lin, W. Chen, H.-J. Wang, Z. Jiang, L. Zheng, T. Yao, J. Dong, S. Wei, W. Huang, L. Gu, J. Luo, Y. Li and Y. Wu, *Nat. Catal.*, 2021, **4**, 134–143.
25 X. Sun, S. Dong and E. Wang, *Chem. Commun.*, 2004, 1182–1183.
26 A. P. Cote, A. I. Benin, N. W. Ockwig, M. O'Keeffe, A. J. Matzger and O. M. Yaghi, *Science*, 2005, **310**, 1166–1170.
27 C. Zhao, X. Dai, T. Yao, W. Chen, X. Wang, J. Wang, J. Yang, S. Wei, Y. Wu and Y. Li, *J. Am. Chem. Soc.*, 2017, **139**, 8078–8081.
28 L. Jiao, W. Xu, Y. Zhang, Y. Wu, W. Gu, X. Ge, B. Chen, C. Zhu and S. Guo, *Nano Today*, 2020, **35**, 100971.
29 Y. Min, X. Zhou, J.-J. Chen, W. Chen, F. Zhou, Z. Wang, J. Yang, C. Xiong, Y. Wang, F. Li, H.-Q. Yu and Y. Wu, *Nat. Commun.*, 2021, **12**, 303.
30 H. Yang, Q. Lin, C. Zhang, X. Yu, Z. Cheng, G. Li, Q. Hu, X. Ren, Q. Zhang, J. Liu and C. He, *Nat. Commun.*, 2020, **11**, 593.
31 P. Giusto, H. Arazoe, D. Cruz, P. Lova, T. Heil, T. Aida and M. Antonietti, *J. Am. Chem. Soc.*, 2020, **142**, 20883–20891.
32 X. Yu, P. Han, Z. Wei, L. Huang, Z. Gu, S. Peng, J. Ma and G. Zheng, *Joule*, 2018, **2**, 1610–1622.
33 Y. Xia, X. Zhao, C. Xia, Z.-Y. Wu, P. Zhu, J. Y. Kim, X. Bai, G. Gao, Y. Hu, J. Zhong, Y. Liu and H. Wang, *Nat. Commun.*, 2021, **12**, 4225.
34 D. M. Koshy, S. Chen, D. U. Lee, M. B. Stevens, A. M. Abdellah, S. M. Dull, G. Chen, D. Nordlund, A. Gallo, C. Hahn, D. C. Higgins, Z. Bao and T. F. Jaramillo, *Angew. Chem., Int. Ed.*, 2020, **59**, 4043–4050.
35 J. Chen, Z. Wang, H. Lee, J. Mao, C. A. Grimes, C. Liu, M. Zhang, Z. Lu, Y. Chen and S. P. Feng, *Mater. Today Phys.*, 2020, **12**, 100176.
36 Z. Wang, J. Fan, B. Cheng, J. Yu and J. Xu, *Mater. Today Phys.*, 2020, **15**, 100279.